PERGAMON

International Journal of Multiphase Flow 26 (2000) 1183–1208

International Journal of Multiphase Flow

www.elsevier.com/locate/ijmulflow

Hydrodynamics of three-dimensional waves in laminar falling films

Philipp Adomeit, Ulrich Renz*

Lehrstuhl für Wärmeübertragung und Klimatechnik, RWTH Aachen, 52056 Aachen, Germany

Received 28 January 1997; received in revised form 14 June 1998

Abstract

Experiments were performed to investigate the flow and surface structure in laminar wavy films over a Reynolds number range from $Re_f = \rho \bar{u} \delta_f / \eta = 27$–$200$. Measurements of the velocity distribution by particle image velocimetry and film thickness by a fluorescence technique enabled to gain detailed information on the transient conditions within the three-dimensional wavy flow. In the entire range of Reynolds numbers, the flow in the wave crest is in a decelerated state, as its momentum is partially transferred into the near wall region, which results in acceleration of the wave back above the equilibrium state. This also affects the residual film behind the waves and causes subsequent waves to collide with their predecessors.

The three-dimensional effects and the wave collision frequency increase with increasing flow rate. Transitions from streak-like to surge-like waves and the development of turbulent spots are first observed to occur at $Re_f \approx 75$. The wave shapes at $Re_f \approx 200$ become completely unsteady and approximately every second wave collision causes the formation of a turbulent spot.

Keywords: Liquid film; Film thickness; Wave structure; Velocity distribution; Experimental data

1. Introduction

Vertically falling films are extensively used in the energy and process industry, e.g. in condensers or falling film evaporators and reactors. Design and operation of these apparatus require a quantitative knowledge of the momentum, energy and mass transfer in the liquid film

* Corresponding author.

0301-9322/00/$ - see front matter
PII: S0301-9322(99)00079-8

phase, since its transfer resistance frequently restricts the performance of the apparatus. Both heat and mass transfer resistance strongly depend on the hydrodynamic mixing induced by the wave motion of the film. This effect has been experimentally proven by many researchers, e.g. Banerjee et al. (1967), Seban and Faghri (1978) and Henstock and Hanratty (1978), which developed empirical heat and mass transfer correlations. All of them, however, are restricted to a certain range of parameters and can hardly be extended to different conditions. To overcome this limitation, the understanding of the hydrodynamics of wavy falling films has to be improved.

This deficiency of knowledge is mainly caused by the lack of sufficiently resolved — both temporally and spatially — velocity data within wavy falling films. Only few measured data of the velocity distribution within falling films are available at present. Unfortunately, these data are either temporally averaged (Ho and Hummel, 1970; Semena and Mel'nichuk, 1978) or single values, not providing information on the transient behaviour (Wilkes and Nedderman, 1962; Nakoryakov et al., 1977; Alekseenko et al., 1985), or are spatially discrete data, which can not be correlated unambiguously to each other and to the shape of the free surface (Mudawar and Houpt, 1993).

Due to the difficulty of direct measurements within wavy falling films theoretical approaches have been used to gain insight into the flow structure. Some analytical models (Alekseenko et al., 1985; Trifonov and Tsvelodub, 1991) assume self-similarity of the velocity profiles in order to calculate the shape of the free surface. This clearly restricts their applicability to small Reynolds numbers. Other analytical models prescribe the geometry of large waves moving over a thin substrate film and derive the flow structure in laminar-wavy (Brauner and Maron, 1983; 1987) or even turbulent (Brauner, 1989) falling films. However, the validity of the underlying assumptions concerning the velocity distribution and the shape of the waves have not been proven.

Numerical solutions do not require such restricting assumptions, since they simultaneously determine the surface shape and the velocity field. Several numerical simulations of the flow structure of laminar-wavy films ($Re_f \leq 300$) have been presented in the last decade. In order to reduce computation time most of them (Bach and Villadsen, 1984; Kheshgi and Scriven, 1987; Ho and Patera, 1990) restricted the computational domain to one wavelength with periodic boundary conditions at both ends and thus achieved results solely for two-dimensional waves remaining in a steady-state with a prescribed wavelength. However, laminar waves do hardly reach such a steady-state due to wave interactions causing a chaotic spectrum of wavelength as seen from the experimental investigations of Takahama and Kato (1980) and Karapantsios and Karabelas (1995). This effect has also been deduced from the long-wave theory by Chen and Chang (1986). Predictions on the flow structure of freely developing and interacting film waves, which overcome the above restrictions, have recently been presented by Stuhlträger et al. (1993, 1995) for the case of film condensation. However, only two-dimensional waves were admitted in their numerical simulation. An earlier three-dimensional numerical analysis by Hagiwara (1989) showed that the interface structure is dominated by three-dimensional waves, exhibiting an elongated drop-like shape. Unfortunately, they interpreted their results only in terms of wave frequency and amplitude and did not attempt to investigate the internal flow structure and its dependence on three-dimensional effects.

Due to the lack of experimental data neither the numerical results nor the conclusions drawn

can presently be verified. Additionally, it remains questionable, whether the predictions of two-dimensional films also describe the flow situation in three-dimensional wavy flow. The present paper aims to supply basic experimental insight into the flow and surface structure of wavy-laminar falling films. The data are necessary to improve the fundamental understanding of three-dimensional wavy flow encountered in most technical applications and are needed to validate the current models.

2. Theoretical considerations

Although this work is focused on experimental results, some basic theoretical considerations shall be undertaken, which are necessary to adequately interpret the measured velocity fields. The flow of isothermal and laminar falling films is described by the equations of continuity and of momentum. The momentum equation in the direction x of gravity is given by

$$\frac{\partial u}{\partial t}+u\frac{\partial u}{\partial x}+v\frac{\partial u}{\partial y}+w\frac{\partial u}{\partial z}=-\frac{1}{\rho}\frac{\partial p}{\partial x}+\frac{\eta}{\rho}\left(\frac{\partial^2 u}{\partial x^2}+\frac{\partial^2 u}{\partial y^2}+\frac{\partial^2 u}{\partial z^2}\right)+g \tag{1}$$

and those in the direction y normal to the solid surface and in z normal to the x–y plane are analogous. The velocity components are u, v and w in x, y and z-direction, respectively. The fluid viscosity is denoted by η, the fluid density by ρ, g is the gravitational constant and p the pressure. The boundary condition at the solid wall is the no-slip condition, while the boundary conditions at the free surface are derived from the balance equations of the tangential and normal stresses. A complete set of continuity and momentum equation and the corresponding boundary conditions can be found elsewhere (Wehausen and Laitone, 1960).

For the special case of a fully developed falling film with a smooth liquid surface, i.e. complete equilibrium of viscous and gravity forces, the above equations have been solved by Nußelt (1916), yielding a parabolic velocity distribution

$$u=\frac{\rho g}{2\eta}\delta_f^2\left(2\frac{y}{\delta_\mathrm{f}}-\left(\frac{y}{\delta_\mathrm{f}}\right)^2\right). \tag{2}$$

From this expression a relation between the film Reynolds number Re_f, which is proportionally to the mass flow rate per unit width $\dot{m}'$, and the film thickness δ_f is obtained

$$Re_\mathrm{f}=\frac{\rho\bar{u}\delta_\mathrm{f}}{\eta}=\frac{\dot{m}'}{\eta}=\frac{1}{3}\frac{\rho^2 g\delta_\mathrm{f}^3}{\eta^2}. \tag{3}$$

The wall shear stress τ_w can also be expressed in terms of the film thickness δ_f by

$$\tau_\mathrm{w}=\rho g\delta_\mathrm{f}. \tag{4}$$

These quantities characterise the hydrodynamic condition and are useful in our case for comparison to measured values. In particular they enable to identify accelerated or decelerated flow regions.

In order to quantify the difference between measured velocity data and the Nußelt solution a

deviation parameter a_{dev} is defined by rearranging Eq. (1)

$$a_{dev} = \frac{\eta}{\rho}\frac{\partial^2 u}{\partial y^2} + g = \frac{\partial u}{\partial t} + \left(u\frac{\partial u}{\partial x} + v\frac{\partial u}{\partial y} + w\frac{\partial u}{\partial z}\right) - \frac{\eta}{\rho}\left(\frac{\partial^2 u}{\partial x^2} + \frac{\partial^2 u}{\partial z^2}\right) + \frac{1}{\rho}\frac{\partial p}{\partial x}. \tag{5}$$

In the two-dimensional equilibrium state, where gravity and viscous forces balance each other, its value is $a_{dev}=0$, which is the inherent assumption of Nußelt's solution Eq. (2). Since the PIV-technique enables to measure velocity data in the x–y plane, it is possible to extract values of $\partial^2 u/\partial y^2$ as a function of y, and thus obtain a quantitative measure of the deviation between the experimentally investigated wavy film and a smooth fully developed film.

As seen in Eq. (5) a_{dev} is affected by various influences, which are the temporal change of momentum, the convective momentum transfer in all three dimensions, the viscous momentum transfer in x and z direction and the pressure gradient. Due to the difficulty of separating these influences care has to be taken to interpret the values of a_{dev} in a physically adequate way. An interpretation scheme based on an estimate of the sign of the individual terms of Eq. (5) is given in Table 1. Here the ideal case of a symmetrical elongated wave is considered, as schematically sketched in Fig. 1. This type of three-dimensional wave is frequently observed experimentally, as seen below.

Table 1 considers the conditions at the wave front and at the wave back separately, and it is seen, that most terms change sign once the wave crest has passed the fluid element under consideration. The only exception is the convective momentum transport in the circumferential z-direction, which always causes a negative contribution to a_{dev}. This reveals the three-dimensional effect of fluid elements located at the lateral wave flanks gaining some additional momentum from the more rapidly flowing fluid near the symmetry line $z = 0$.

In the experimental results discussed below, a predominance of negative values of a_{dev} is observed in both wave front and wave back. This can be analysed by considering the individual terms in Table 1. In the wave front, the negative contributions of the pressure gradient and of the convective momentum transfer in x-direction from the approaching wave

Table 1
Scheme of the estimated sign of terms contributing to the deviation parameter a_{dev} in the wave front and in the wave back

Term	Wave front	Wave back
Temporal change $(\partial u/\partial t)$	>0	<0
Pressure gradient $(\partial p/\partial x)$	<0	>0
Convective x-momentum transport $u(\partial u/\partial x)$ in x-direction	$u>0$, $(\partial u/\partial x)<0$: <0	$u>0$, $(\partial u/\partial x)>0$: >0
Convective x-momentum transport $v(\partial u/\partial y)$ in y-direction	$v>0$, $(\partial u/\partial y)>0$: >0	$v<0$, $(\partial u/\partial x)>0$: <0
Convective x-momentum transport $w(\partial u/\partial z)$ in z-direction	$z>0$: $w>0$, $(\partial u/\partial z)<0$: <0	$z>0$: $w>0$, $(\partial u/\partial z)<0$: <0
	$z<0$: $w<0$, $(\partial u/\partial z)>0$: <0	$z<0$: $w<0$, $(\partial u/\partial z)>0$: <0
Viscous forces $(\partial^2 u/\partial x^2)$, $(\partial^2 u/\partial z^2)$	no estimate	no estimate

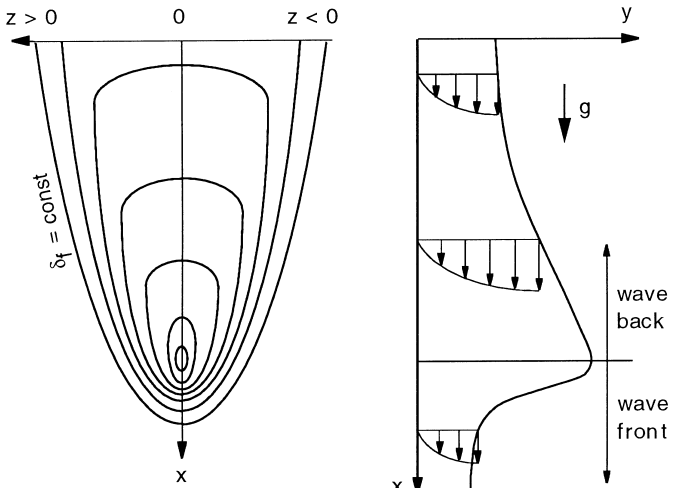

Fig. 1. Schematic description of the streak-like wave considered in Table 1.

crest obviously exceed the positive contributions of the remaining terms including the acceleration $\partial u/\partial t$. In the wave back, negative values of a_{dev} are caused by deceleration and convective momentum transport in the y-direction from the rapidly flowing fluid at the free surface. In both cases negative a_{dev} are additionally supported by the momentum transport in the z-direction from the fluid near the wave symmetry line.

This simple interpretation can hardly be applied to all flow situations observed experimentally, since it is restricted to a steady wave of ideal shape and thus neglects additional effects, arising from wave interaction and deformation.

3. Experimental

3.1. Experimental set-up

A falling film on the inside of a glass tube is provided by a closed-loop apparatus, sketched schematically in Fig. 2. In the range of the Reynolds numbers investigated here, the tube length of 1.5 m is sufficiently long to achieve a wavy falling film, which can be regarded as fully developed e.g. with respect to statistical properties like minimum, mean and maximum thickness (Portalski and Clegg, 1972) and with respect to the development of turbulence (Takahama and Kato, 1980).

The film is generated by a circular gap between a conical bore and a cylindrical piston adjustable in both axial and radial direction. Upon feeding the film carries less momentum than a fully developed film, since the gap width, which is varied between 0.25 and 0.55 mm for $Re_{\mathrm{f}} \approx 30$–$200$, approximately equals the film thickness of a fully developed smooth film. The entrance momentum is intended to reduce the tube length needed for flow development. In order to avoid circumferential maldistribution of the liquid film the radial displacement between piston and bore has been aligned to an accuracy of 0.01 mm.

At the end of the glass tube the film fluid flows into a reservoir equipped with heating and cooling devices to control a constant fluid temperature. The film fluid is circulated by a magnetically driven centrifugal pump and its flow rate is adjusted by a valve–bypass combination and measured by a rotameter. A partially filled vessel is used to dampen pressure fluctuations caused by the centrifugal pump and simultaneously to deaerate the film fluid by ultrasonic agitation. A second bypass loop enables to clean the film fluid from tracer particles by circulating it through a filter combination with a pore size of 0.3 μm.

Two types of glass tubes were used in this investigation. Duran glass tubes of 46 mm ID were used for film velocity measurements with particle image velocimetry. Quartz tubes with a slightly larger ID of 54 mm were used for fluorescence intensity imaging. The enlargement of the diameter allows to extend the measurement area. However, no differences in the wave structure could be observed in comparison to preliminary tests with the smaller ID. Measurements were generally undertaken at a location 1.4 m downstream of the film distributor. The measurement techniques are described in the following sections.

3.2. Measurement of the velocity distribution

A particle image velocimetry (PIV) system is used here to determine the fluid velocity distribution within the wavy falling film. The PIV technique has been chosen since it provides

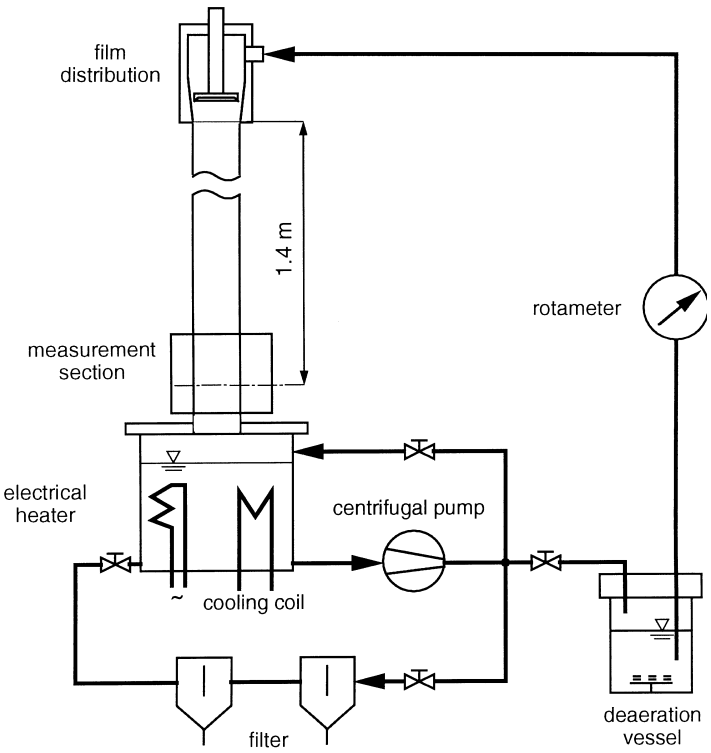

Fig. 2. Schematic of the experimental set-up.

information on the instantaneous velocity field and thus is significantly better suited for the application to a transient flow than spatially discrete measurement systems such as LDA. In transient flow situations spatially discrete measurements, recorded at subsequent times, can hardly be correlated to each other in order to determine the instantaneous flow situation, as it is necessary to understand the hydrodynamic structure of wavy falling films.

The PIV-system, sketched schematically in Fig. 3, consists of the light sheet generating optics and a CCD-camera for image recording. It is positioned in a way that its measurement plane is parallel to the tube axis and extends normal to the tube wall. In this position both the film velocity components in the mean flow direction u and normal to the wall v can be determined as a function of the distance from the tube wall.

The major difficulty in using an optical measurement technique to investigate the flow within thin liquid films is to gain a good optical access without distorting the film flow. In the present work, this problem was solved by using a fluid whose refractive index is matched to the glass tube. Dimethylsulfoxide (DMSO) is used as the film fluid, which meets this optical demand when kept at a temperature of 37°C. Refractive index matching by mixing fluids was excluded a priori, since surface tension differences between different compounds may induce convective motions at the free surface, known as Marangoni convection, which influence the flow as well as the surface structure in an unpredictable manner. At 37°C DMSO has a density of $\rho = 1084$ kg/m^3, a viscosity of $\eta = 1.64\ 10^{-3}$ Pa s and a surface tension of $\sigma = 0.042$ N/m^2.

The microscopical PIV-system used here has specially been designed for the application in thin liquid films with a thickness well below 1 mm. Multiple exposure of the tracer particles, which are $ZrSiO_4$-particles (mean diameter $d_{50} = 1.8$ μm, maximum diameter $d_{95} = 4.0$ μm, density $\rho_p = 4560$ kg/m^3, refractive index $n_p = 1.98$) is achieved by a novel illumination technique. The beam of a 5 W-cw-Ar-ion-laser is shifted parallel by a rotating glass octagon, generating a very small light sheet of high and homogeneous intensity. The illumination repetition rate ranges up to 3 kHz, which corresponds to a beam scanning velocity of approximately 35 m/s. Focusing of the laser beam by expansion–collimation optics results in a beam waist with a diameter of 40 μm.

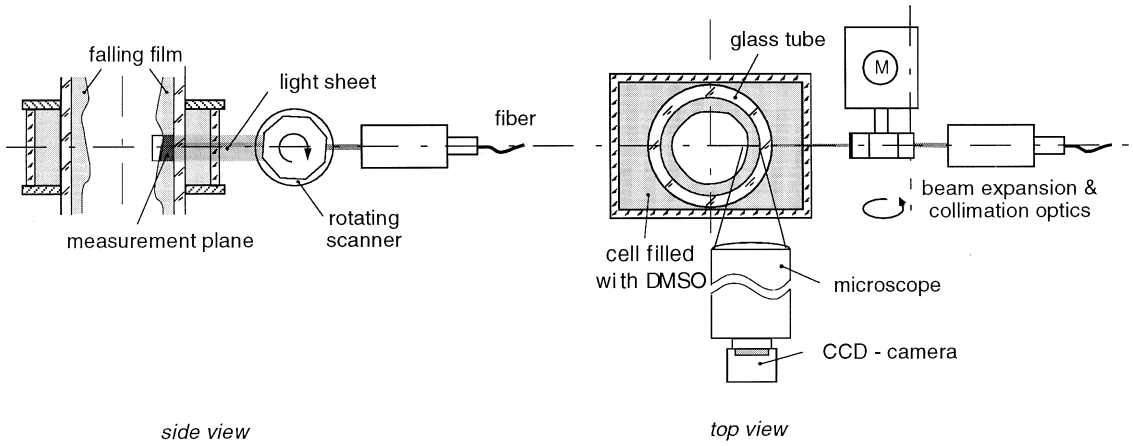

Fig. 3. Schematic of the particle image velocimetry system.

The scattered light of the tracer particles is recorded by a CCD-camera connected to a microscope with both long focal distance and good numerical aperture. The camera signal is stored on a S-VHS video system for further evaluation on a digital image processor. The PIV-evaluation is based on a modified autocorrelation algorithm described in detail elsewhere (Adomeit, 1996). The electronic shutter of the CCD-camera is set to control the exposure time in the range between 2 and 4 ms, which was found to be short enough to achieve a quasi-steady flow field during exposure.

A typical frame recorded in a wave trough and the velocity distribution evaluated by the PIV-technique are shown in Fig. 4(a) resp. (b). Each tracer particle is illuminated up to five times, which results in a chain-like trace of its motion. Such traces can be seen most clearly in the low velocity region close to the tube wall, marked by 'A' in Fig. 4(a). Near to the free surface some strongly blurred particle images are observed. These distorted images are caused by total reflection at the liquid–gas interface, since the film liquid has a higher refractive index then the gas above it. This phenomenon allows accurate determination of the location of the free surface, when both the images of the tracer particles and their reflections are recorded on the frame.

In the example Fig. 4(a) the information on the instantaneous film thickness can be obtained from two particles very near to the free surface, 'B' and 'C', but also from a configuration of particles marked by 'D'. This method of determining the film thickness has been found to be generally applicable to all frames recorded. Its accuracy depends to some degree on the statistical fluctuations in the spatial distribution of tracer particles near the free surface, but is always better than 20 μm.

Figure 4(a) also shows that the velocity component parallel to the wall remains constant within the small size of the measurement area. For this reason the velocities are displayed as one-dimensional velocity profiles, such as given in Fig. 4(b), which provide all information without any losses. Furthermore, it is found that the velocity component normal to the tube wall is too small to be evaluated accurately, since the particle displacements in this direction are of the same magnitude as the microscope resolution. Hence, results of the normal velocity component v were excluded from presentation.

The measurement accuracy of the microscopical PIV-system depends on the error in determining the length of the displacement vector between two particle illuminations, which is

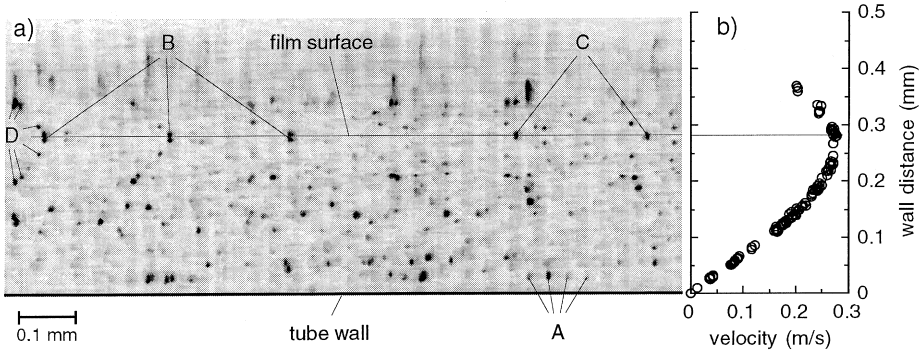

Fig. 4. (a) Typical frame recorded by the PIV-system, (b) velocities evaluated from (a).

proportional to the particle velocity, and on the basic system error originating from the evaluation procedure, from the uncertainty in optics calibration and from the timing fluctuations of the illumination system. Since the image is processed with sub-pixel accuracy, it is a rather conservative estimation that the particle displacement vector length is obtained with an uncertainty of the effective resolution Δx in the flow direction of the imaging system. The error evoked by the restricted resolution depends on illumination rate, magnification and flow velocity, whereas the basic system error due to timing fluctuations of the illumination system and optics calibration can be regarded as constant and is estimated to be smaller than 2%. In Table 2 the resulting relative error is given for the parameters chosen in the present experimental runs.

The error estimation has been proven valid by measurements in a developing laminar flow between parallel plates. For this geometry the velocity distribution can be calculated theoretically and provides an exact basis for comparison to the data obtained by the microscopical PIV-system. The comparison of theoretical and PIV-data, given in Fig. 5 shows, that the observed measurement errors are well within the expected range as given in Table 2.

Furthermore, the measurements in the parallel plate channel enable to check the quality of the procedures used to evaluate the wall shear stress τ_w and the deviation parameter a_{dev} defined in Eq. (5). Both quantities require to evaluate spatial derivatives of the measured velocity distribution, which requires the use of a suitable method to avoid amplification of measurement scatter by differentiation. Here the method of approximate splines has been applied. Its weighing factors are optimised by an automated numerical procedure in order to gain a good fit to the measured without amplifying scattering generated oscillations of the second derivative $\partial^2 u/\partial y^2$.

Figure 6 compares results of this evaluation procedure to exactly known distributions of a_{dev}. Figure 6(a) shows the results obtained in the parallel plate experiment (plotted as a_{dev}–g, since the flow is pressure, and not gravity driven) in comparison to the exact theoretical values.

Table 2
Error estimation of the PIV-measurements in the present experimental runs

Experimental run	$Re_f = 30$	$Re_f = 77$	$Re_f = 200$	Parallel plate
Magnification	6.8	5.4	5.4	3.7
Illumination rate (Hz)	2940	2750	3020	1120
Effective resolution Δx (μm)	2.4	3.2	3.2	4.4
Effective resolution Δy (μm)	3.2	4.1	4.1	5.9
Velocity (m/s)	estimated relative error (%)			
0.1	8.9	10.6	11.5	6.7
0.2	5.3	6.2	6.6	4.2
0.3	4.2	4.7	5.0	3.4
0.4	3.6	4.0	4.2	3.0
0.5	3.2	3.6	3.7	2.8
0.6	3.0	3.3	3.4	2.6
0.8	2.7	2.9	3.0	2.4
1.0	2.5	2.7	2.8	2.3
1.5	2.3	2.4	2.4	2.1
2.0 m/s	2.2	2.2	2.3	2.0

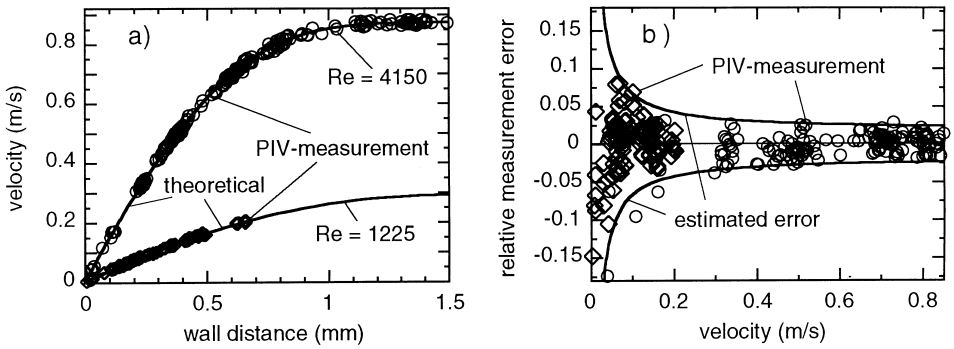

Fig. 5. (a) Velocity distribution in a developing parallel plate flow, (b) comparison between experimentally observed and estimated measurement error.

A further check of the procedure was performed by evaluating data generated by superimposing velocity scatter of the magnitude of the measurement error at $Re_f = 77$ and location scatter of the magnitude Δy simultaneously onto velocity profiles obtained from a numerical simulation of wavy film flow with a spectral element method by Adomeit (1996). Figure 6(b–d) shows examples of these data and the distribution of a_{dev} evaluated from it in comparison to the numerical values. The numerical values of a_{dev} and the results obtained by differentiation of the approximate spline functions are in a rather good agreement. The maximum differences observed in a large number of tests are about 3 m/s^2 in the region of vanishing velocities near the wall, but decrease to 2 m/s^2 in the free flow, where $u > 0.1$ m/s.

Considering the wall shear stress τ_w the maximum difference between the theoretical or

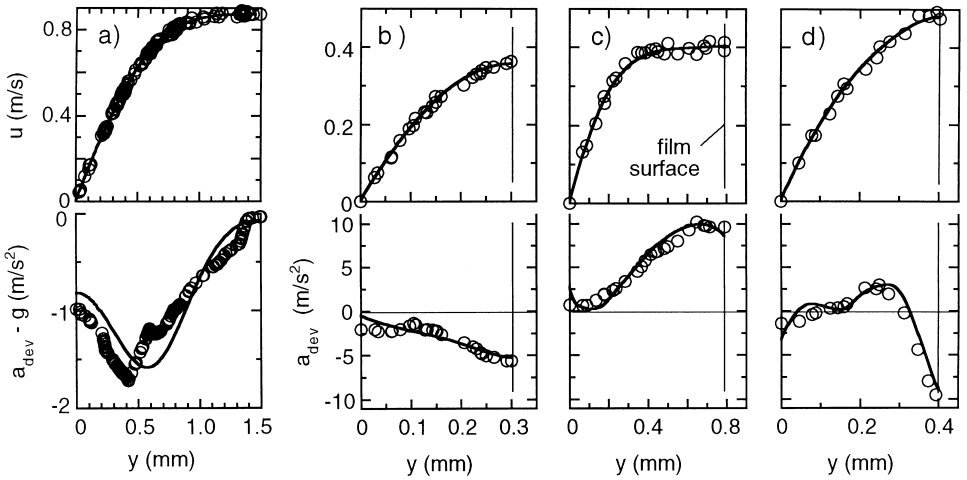

Fig. 6. Distribution of flow velocity u and deviation parameter a_{dev}: (a) parallel plate flow data, (b–d) numerical 2D-wavy film flow data upper series u: (–) exact in (a), original numerical data in (b–d) (○) measured in (a), scatter superimposed in (b–d) lower series a_{dev}: (–) exact in (a), numerical distribution in (b–d) (○) evaluated with Eq. (5) from the (○) velocity data.

numerical values and the values evaluated from the spline functions approximating the velocity data is smaller than 7%.

3.3. Measurement of the transient film thickness distribution

PIV-measurements provide the transient velocity distribution within a spot of a wavy film. However, the PIV-data are difficult to interpret without general information on the flow structure, e.g. the wave shapes and their interactions. In order to gain such information an experimental technique has been developed, which enables determination of the instantaneous film thickness distribution in an area of approximately 30×200 mm^2. This novel fluorescence intensity imaging technique, shown schematically in Fig. 7, is based on the relation between the thickness of a layer of a fluorescent liquid and its fluorescence intensity. A similar technique has previously been used by Liu et al. (1993) to visualise the occurrence of instabilities in inclined film flows.

As a fluorescent tracer a small amount of sodium-fluorescine ($C_{20}H_{10}Na_2O_5$) is added to the film liquid DMSO in a mass fraction of 8×10^{-4}, so that it does not affect the physical properties of DMSO. Sodium-fluorescine exhibits a bright orange fluorescent light, if excited with UV-light of 300–360 nm wavelength. A high-pressure mercury-vapour lamp equipped with a black-glass filter is used as the UV-source, the light of which is focused by cylindrical quartz-optics to achieve a thick and almost parallel light sheet incident at an angle of $0 \pm 3^\circ$ normal to the tube axis, which covers the complete measurement area.

The fluorescent light emitted by the film fluid is recorded by a CCD-camera equipped with an UV-filter, which cuts off all directly reflected or scattered UV-light. Shutter intervals of less than 1 ms ensure that image distortion due to surface motion is negligible. The frames are stored on a MII-video recorder. Subsequent digital image processing corrects for the non-homogenous distribution of the UV-illumination and converts brightness into film thickness

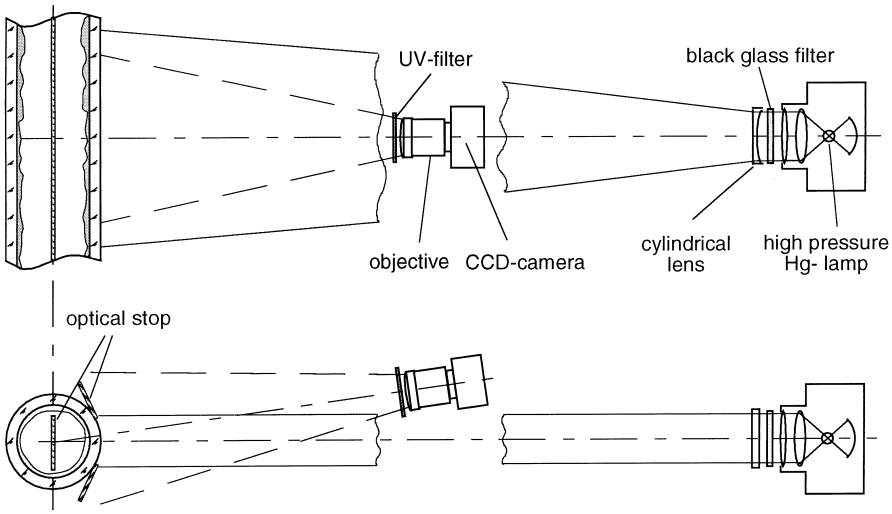

Fig. 7. Schematic of the fluorescence intensity imaging system.

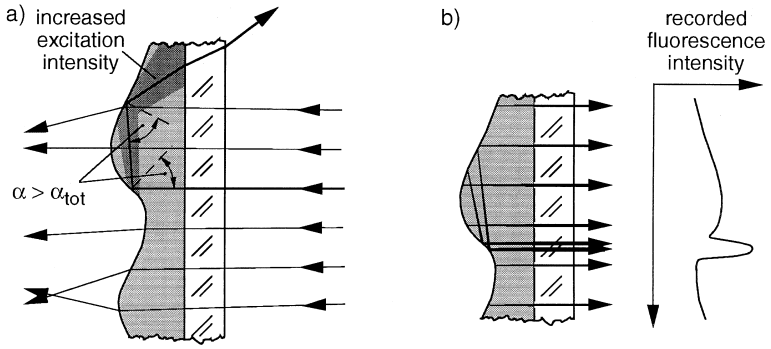

Fig. 8. Effects of total reflections of (a) UV-light and (b) fluorescence light on the recorded fluorescence intensity.

distributions. Both processing steps are based on calibration data obtained by recording the fluorescence intensity of a sample of film liquid in either an planar cell with 1 mm gap width or an wedge shaped cell with a calibrated gap width varying from 0 to 1.2 mm along its length, which are positioned at the same location as the glass tube and thus are exposed to the same UV-illumination.

The measurement error of this method is approximately 0.04 mm. The main error sources are the CCD-sensor noise and the imperfections of the fitted two-dimensional polynomial functions used to correct the UV-intensity distribution, which cause an error of approximately 0.02 mm. The dependence of fluorescence intensity on film thickness can be obtained accurately within ± 0.005 mm. The error due to tube surface curvature is diminished by refraction and is calculated to be 0.02 mm.

A further measurement error is caused by total reflection of both fluorescent and UV-light at the free surface. This effect is restricted to extremely inclined wave fronts where the angle between interface surface and incident light exceeds $\alpha_{tot} = \arcsin\ (n_{air}/n_{DMSO}) = 46.6^{\circ}$, as sketched in Fig. 8. The consequence of UV-reflection is an increase of the excitation intensity around the reflecting spot, which is restricted by the high UV-absorption of the film liquid to an extension of roughly 1 mm. Total reflections of the fluorescent light have a stronger influence, since light of this wavelength is not adsorbed by the film liquid. Hence, the recorded fluorescence intensity at a reflecting spot is significantly increased above the level of its surrounding and thus can be easily detected and excluded from evaluation.

Although the loss of information at total reflecting spots is certainly a disadvantage of the fluorescence intensity imaging technique, it is partially compensated by the ability of identifying steeply inclined surface areas easily, which greatly helps to identify spots of turbulent motion within the film, as seen from the results discussed below.

4. Results and discussion

4.1. Structure of three-dimensional waves

The wave structure of the falling film has been investigated by fluorescence intensity imaging

at Reynolds numbers in the range between $Re_f = 27$ and $Re_f = 196$. In previous investigations (e.g. Karapantsios et al., 1989) statistical results of scalar quantities like wave amplitude, frequency and propagation velocity have been presented in detail. This paper intends to present exemplary results on the temporal development of the two-dimensional film thickness distribution $\delta_f(x, z, t)$, which give insight into the wave patterns, their motion and interaction. Such information is essential to interpret the velocity measurements which have been made in addition.

At $Re_f = 27$ most waves are bent to an U or W-shape, as shown in a frame sequence in Fig. 9. Elongated waves, whose extension in the mean flow direction x is significantly larger than in the circumferential z-direction, are observed rarely, e.g. the waves marked 'C' and 'D'. This type of streak-like wave, however, is not stable at this small flow rate. The wave 'C' is strongly decelerated by the substrate film, which leads to a broadening of this wave at t = 60–120 ms. Its spreading mass is collected by the subsequent wave 'E', whose thickness increases significantly with time. The wave 'D' also disintegrates, as it splits up into two smaller waves at t = 60 ms, which merge again at t = 180 ms.

Wave collisions and separations also occur frequently among the smaller waves, but do not significantly affect the wave shape. Nevertheless, wave interactions induce a circumferential film mass transport, as shown by the merging waves marked 'A' and 'B'. At t = 0 ms they are found to cover the complete frame width, but subsequently their mass is concentrated at the centre of the frame at t = 180 ms. The substrate film covering the area between the waves

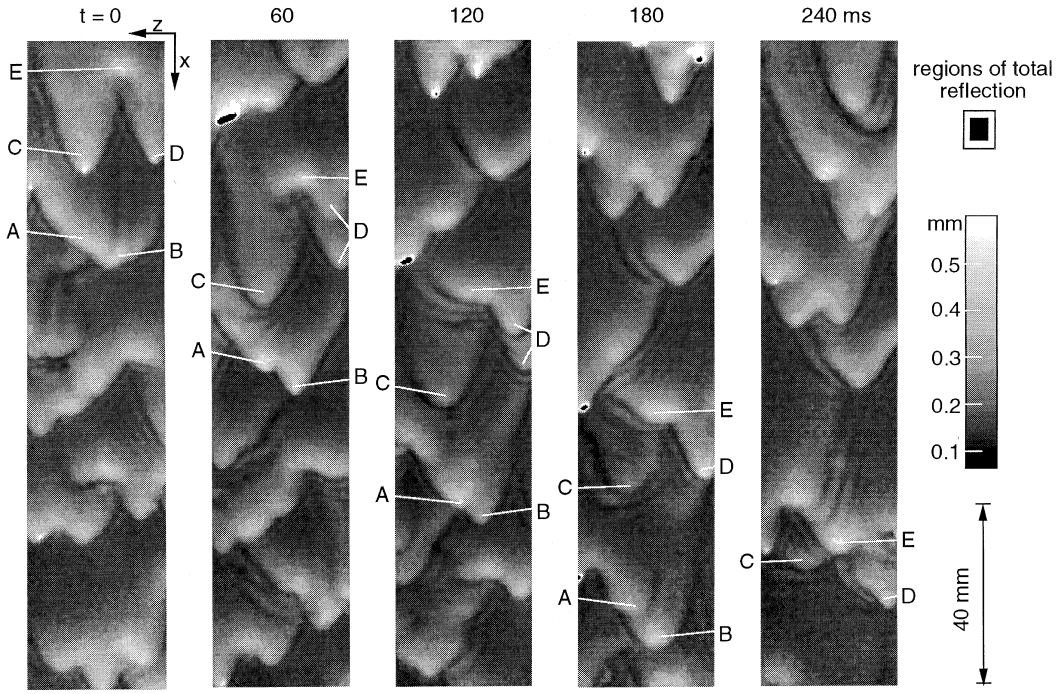

Fig. 9. Temporal development of 3D-wave structures at $Re_f = 27$.

appears smooth and mostly undisturbed, except for the area immediately in front of larger waves, where small capillary forerunner waves are induced.

At an increased flow rate, $Re_f = 72$, the observed span of wave structures ranges from comparatively regular small waves, similar to those at $Re_f = 27$, to the onset of turbulent spots, which generally is expected at significantly higher Re_f. The predominant wave shape, however, is that of elongated streak-like waves, as seen from three frame sequences given in Fig. 10.

At this increased flow rate wave collisions occur more frequently and result in waves accumulating a large fluid mass. Their stability is mainly determined by the type of flow interaction, which they experience. When interacting solely with thin substrate film, such accumulated waves disintegrate again, as seen in Fig. 10, sequence I. The waves marked 'A', 'B' and 'C' form a wave conglomerate at $t = 40$ ms. Subsequently the waves 'A' and 'B' separate from this conglomerate, since they develop a higher velocity than wave 'C', which is slowed down by the interaction with thinner and slower substrate film in front of it.

When multiple collisions with smaller waves occur, wave conglomerates even increase in size, as observed in sequence II of Fig. 10. Here, four waves, 'D'–'G', merge to a surge-like wave at $t = 40$ ms, which due to its significantly larger velocity collides into the elongated waves 'B' and 'C' at $t = 80$ ms. A further collision of its parts 'B' and 'D' with the preceding wave 'A' is to be expected at $t > 80$ ms, leading to an increase in mass, but probably also to an elongation of this surge-like wave.

Such large waves of course can affect the local flow structure in a way, which is expected to occur only at higher Re_f. The onset of turbulence at a strongly decelerated wave part, which is observed in sequence III of Fig. 10, is a singular event in an amount of several thousand frames recorded at $Re_f = 72$. At $t = 40$ ms an exceptional large streak-like wave, marked 'C', collides into the lateral flank of a preceding smaller wave 'A'. The film surface within the collision area is strongly deformed, which induces total reflections at several closely spaced locations. Since total reflections require the surface to exceed an inclination of approx. 35°, this observation can only be explained by the formation of turbulent vortices due to high local shear stresses. As seen at $t = 80$ ms, the turbulent wave tip 'T' propagates at a smaller velocity than the laminar wave tip 'C', obviously due to the enhanced momentum transfer between surface and wall flow induced by turbulence. Consequently, the wave separates at its left flank, which induces a significant broadening of 'C' and also deforms the co-current wave 'B'.

The observed heterogeneity of the flow conditions is probably one reason for the enhancement of heat and mass transfer compared to a smooth film. A second reason is the permanent distortion of the substrate film by the waves motion. Even large areas of thin substrate film, as shown in sequence II, are not smooth and appear severely distorted. The remarkable strainy structure is probably caused by the deceleration, which the flow at the back of the surge-like wave experiences.

At $Re_f = 196$ the wave patterns become less heterogeneous. Here laminar streak-like waves occur intermittently with partially turbulent streak-like waves or larger turbulent surge-like waves. Four sequences, presented in Fig. 11, provide an overview over the typical wave patterns. Turbulence is found to be frequently induced by the deceleration of rapid streak-like waves, once they directly interact with slow substrate film, as seen in sequence I and II of Fig. 11.

The formation of a small turbulent area, shown in sequence I, is comparable to that at

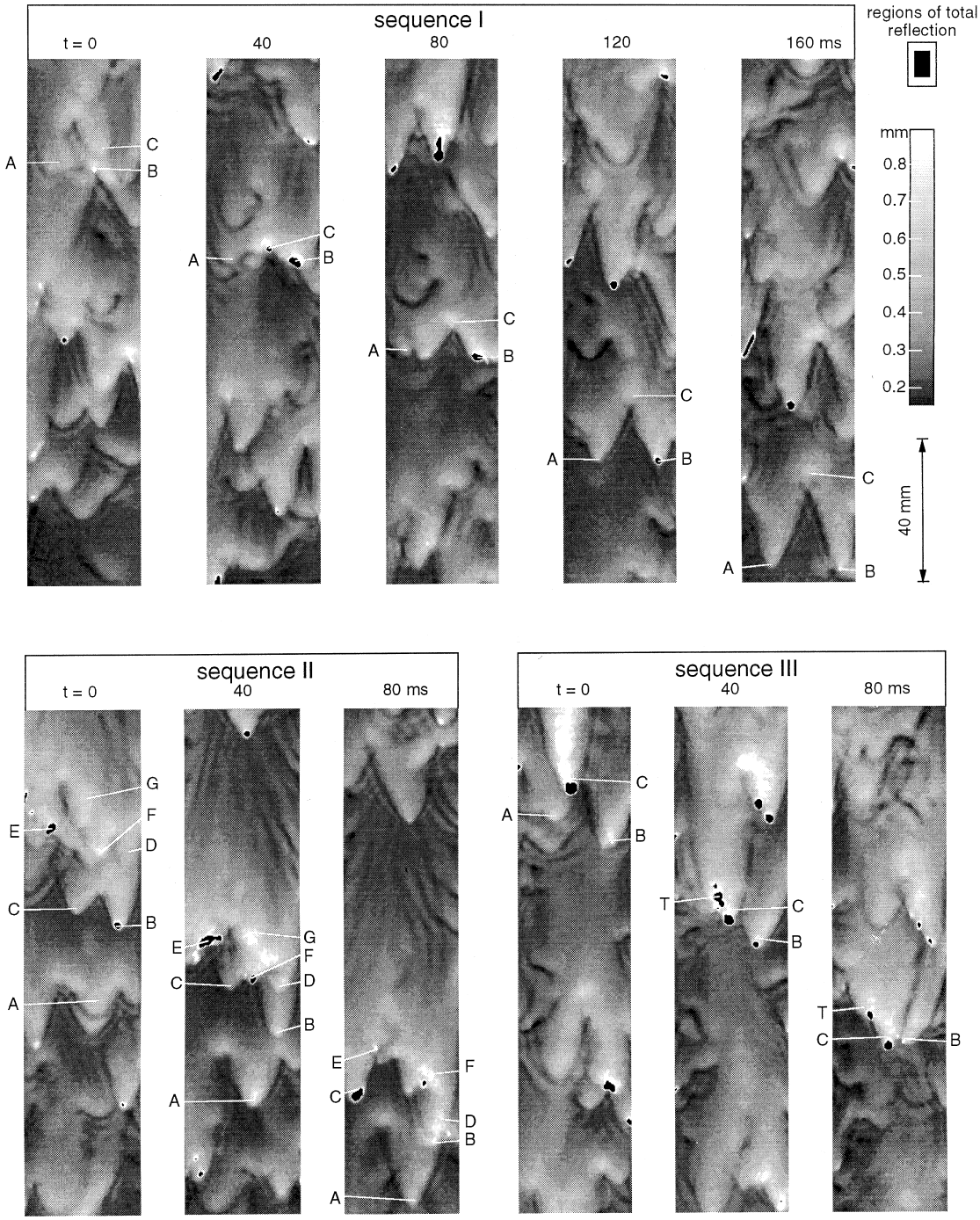

Fig. 10. Temporal development of 3D-wave structures at $Re_f = 72$.

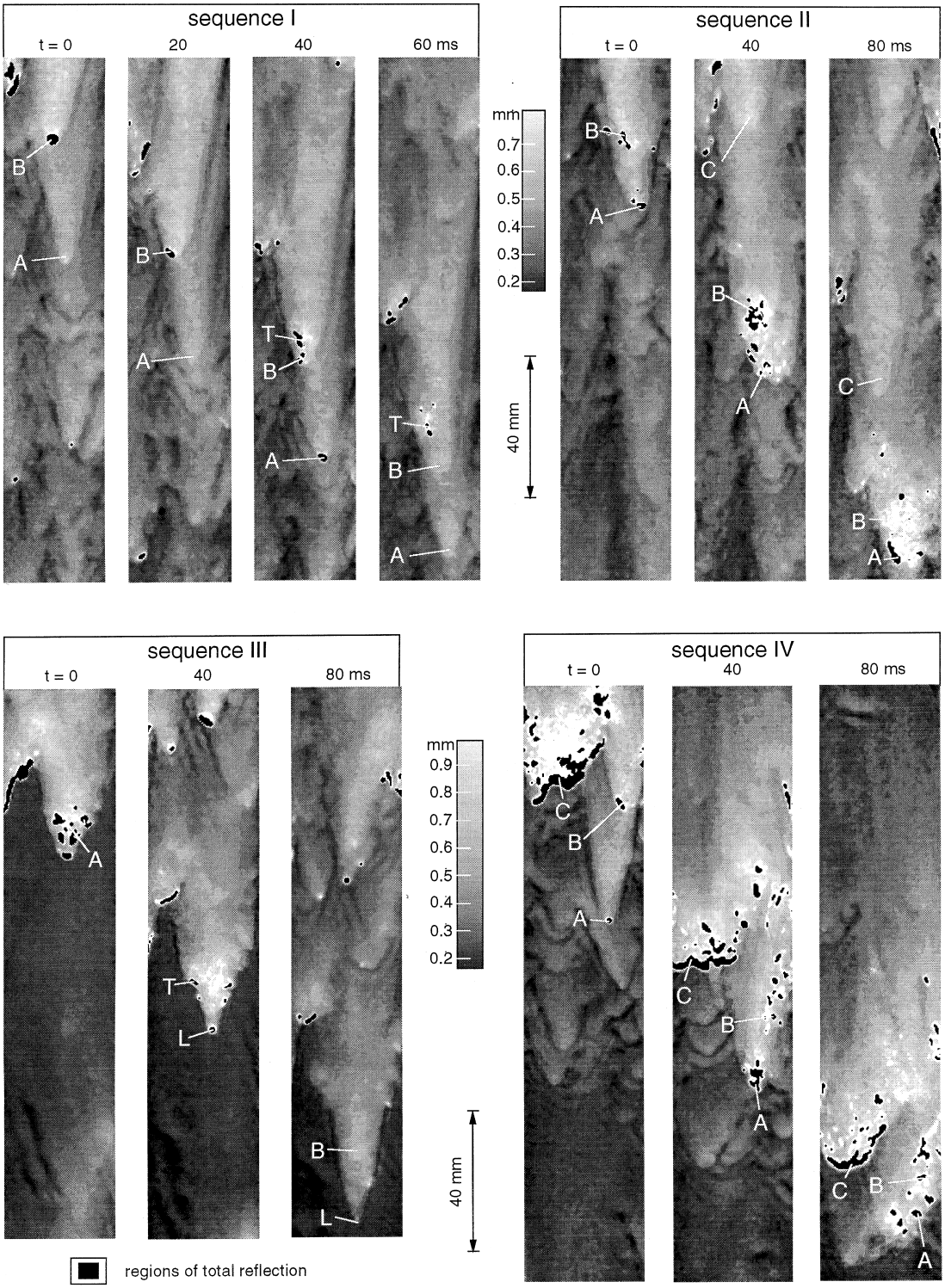

Fig. 11. Temporal development of 3D-wave structures at $Re_f = 196$.

$Re_f = 72$ (seq. III in Fig. 10). A turbulent spot, marked 'T', is induced by the deceleration of the laminar streak-like wave 'B', when it overruns the preceding streak-wave 'A' and hits the thin substrate film at the left flank of A at $t = 40$ ms. Subsequently the wave splits into a laminar wave tip 'B' and a small turbulent region 'T', which due to the turbulent momentum exchange moves at a significantly smaller velocity than the laminar tip 'B'. Sequence II of Fig. 11 shows the onset of turbulence in the tip area of two consecutive laminar streak-like waves, marked 'A' and 'B', after collision with thin and slow substrate film at $t = 40$ ms. Subsequently this turbulent region decelerates and spreads out.

The inspection of several thousand frames has shown that about 50% of all streak waves remain laminar at $Re_f = 196$ and have a similar appearance as those shown in sequence I, since they tend to slide down in the wake of their predecessor. Direct interactions with slow substrate film, necessary to induce turbulence at this Re_f, occur rarely. Furthermore, turbulent regions relaminarise rapidly, unless they are energised by additional wave interactions. An exemplary relaminarisation process is shown in sequence III of Fig. 11. The turbulent wave 'A', sliding onto a large area of undisturbed substrate film, splits into a laminar wave tip 'L' and a turbulent region 'T' at $t = 40$ ms. At $t = 80$ ms the turbulent region relaminarises and forms a secondary wave 'B', following the tip 'L'.

The reduction of the velocity of turbulent waves due to the additional turbulent momentum exchange causes collisions of subsequent laminar waves with turbulent areas. Thereby turbulent surge-like waves of growing mass develop, which finally achieve a sufficiently large velocity to overrun smaller laminar waves. An exemplary surge-like wave is shown in sequence IV, marked 'C'. It initially merges at its right flank with a laminar streak wave 'B', which follows the streak-like wave 'A'. At $t = 40$ ms 'A' and 'B' turn turbulent due to direct interaction with slow substrate film and decelerate significantly. By overrunning several small substrate waves at $t = 80$ ms the turbulent surge 'C' increases in velocity. A subsequent collision of the waves 'A', 'B' and 'C' is to be expected, which will further enlarge the turbulent surge. However, surge waves of this size are rare, since they require a statistically improbable sequence of subsequent wave collisions to be generated.

4.2. Velocity distributions in wavy films

Velocity distributions within the wavy flow were measured in sequences of 14–16 subsequent frames in time increments of 20 ms by the PIV-technique. Coherent sequences of this length are difficult to obtain because of the frequent occurrence of frames with non-homogeneous distribution of tracer particles or significant velocity components in the circumferential direction, which can not be evaluated properly by the PIV processing. A general restriction in the interpretation of the sequences is caused by the short camera shutter intervals of, respectively 2 and 4 ms. Hence, the velocity distribution is evaluated only during 10–20% of the overall sequence duration and information on the flow structure in between the frames is not available.

Figure 12 shows a sequence of velocity profiles and corresponding film thicknesses measured at $Re_f = 30$ ($\dot{m}' = 0.049$ kg/s m). The measured velocity profiles are fitted by approximate splines as discussed in Section 3.2 and compared to Nußelt velocity profiles Eq. (2) for the measured film thickness δ_f. A comparison to Nußelt theory allows to quantify the local

deviation of the measured velocities from the ideal velocity distribution in equilibrium of gravity and viscous forces in a film of negligible surface curvature.

Additional information extracted from the velocity measurements is given in three further graphs. The uppermost graph displays the instantaneous film flow rate $\dot{m}'^*$ obtained by integration over the measured velocity profile and the corresponding value $\dot{m}^*_{\mathrm{Nu}}$ calculated from Nußelt theory by evaluating Eq. (3) with the measured instantaneous film thickness δ_{f}. The second graph shows the temporal development of the instantaneous wall shear stress τ^*_{w} obtained by differentiation of the approximate splines fitting the measured profile at $y = 0$ and the Nußelt value τ_{w^*Nu} evaluated by Eq. (4) with δ_{f}. Further spatially resolved information is given by the distribution of the deviation parameter a_{dev}, obtained by evaluating Eq. (5) with the approximate spline functions as discussed in Section 3.2. Hence, this figure shows the integral deviation, the wall gradient and the locally resolved deviation between the measured and the corresponding Nußelt profiles.

Four waves pass the measurement area at regular time intervals during the sequence in Fig. 12, the first three of them being of comparable height, $\delta_{\mathrm{f}} = 0.47$–$0.56$ mm, while the last is significantly smaller. A large part of the film fluid is transported within the three large wave

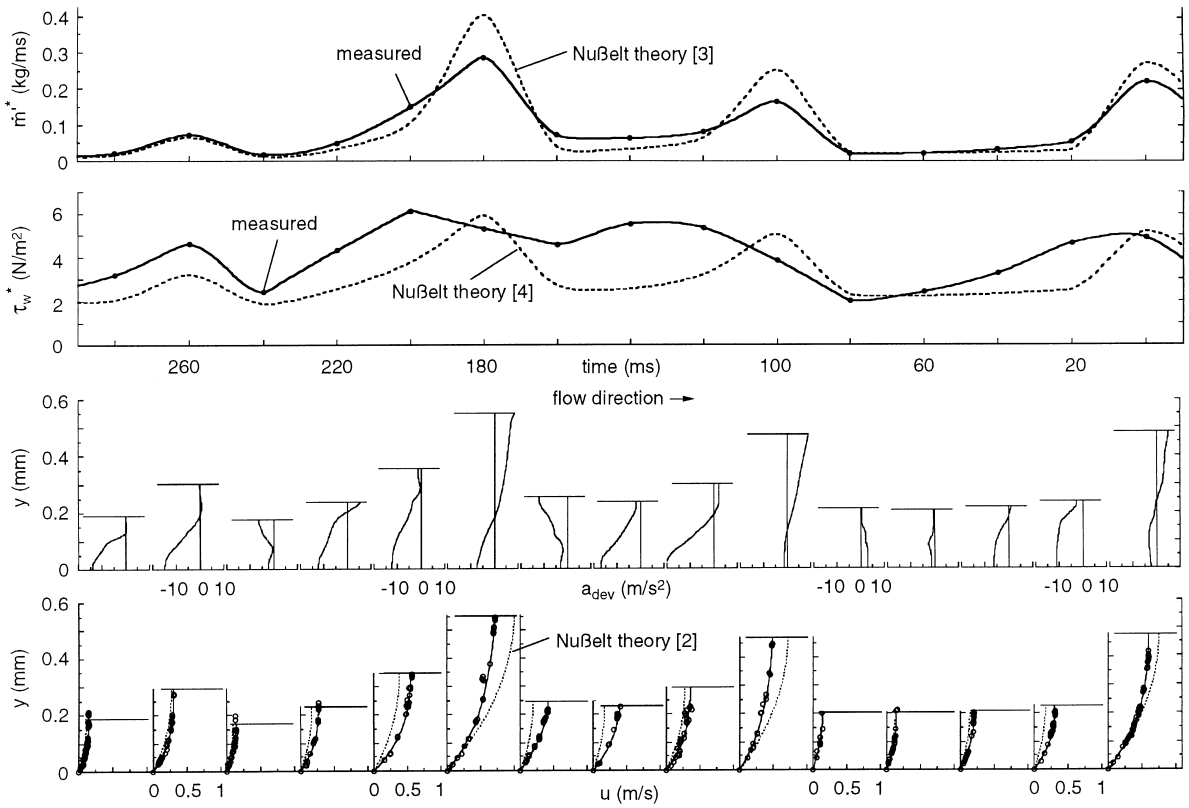

Fig. 12. Profiles of velocity u compared to the corresponding Nußelt profiles Eq. (2), profiles of deviation parameter a_{dev} and the comparison between the local mass flow rate $\bar{m}'^*$ and wall shear stress τ^*_{w} to the corresponding $\bar{m}^*_{\mathrm{Nu}}$ and $\tau_{\mathrm{w^*Nu}}$, as calculated from Nußelt theory Eqs. (3) and (4) in their temporal development at $Re_{\mathrm{f}} = 30$.

crests, where the instantaneous flow rate $\dot{m}'^*$ reaches a maximum of 0.29 kg/(s m) at $t = 180$ ms. In the residual film, whose thickness ranges from $\delta_f = 0.18$–0.25 mm, the flow rate is as small as $\dot{m}'^* = 0.017$ kg/(s m).

In a qualitative manner the measured velocity profile appear to be parabolic throughout the complete sequence. However, they largely differ from the Nußelt profiles, which reveals that there is hardly an instant at which the wavy film flow is in a simple equilibrium of viscous and gravity forces. Obviously internal momentum transfer affects the flow as much as the external gravity forces. Some characteristic attributes of the internal momentum transfer can be observed. First the flow within the crests of the large waves is considerably slower than in equilibrium of gravity and viscous forces, as seen from the velocity profiles and the instantaneous $\dot{m}'^*$, which are approximately 25–40% smaller than the corresponding Nußelt values $\dot{m}^*_{Nu}$. In conjunction with the positive values of a_{dev} at the wave top, this can be interpreted by transfer of x-momentum from this region into its surrounding accordingly to Table 1.

A second characteristic is observed in the wave back, where the flow velocity is generally significantly higher than it would be in equilibrium of gravity and viscous forces. The measured surface velocity u_s is more than twice that predicted by Nußelt theory and consequently the local mass flow rate $\dot{m}'^*$ exceeds $\dot{m}^*_{Nu}$ by up to 90%. The temporal development of the experimentally observed wall shear stress τ^*_w shows a third characteristic attribute. Most interestingly, the maximum of τ^*_w does not occur in the wave crests, but with a delay of 20–40 ms in the back of the waves. In the wave back the deviation parameter a_{dev} is negative throughout the film with an extreme at the wall. Obviously an excess of momentum is transferred into the wall region from adjacent fluid of higher momentum. The lagging of the wall shear stress seems to be a consequence of the delayed reaction of the near wall flow due to its inertia on the momentum transfer from the fast flow region at the wave top.

Considering the temporal evolution of the velocity distribution it is seen that in the back of the first wave the excess of velocity (compared to the Nußelt profile) diminishes with time. Finally at $t = 80$ ms the substrate film converges to an undisturbed state and exhibits a velocity profile identical to the Nußelt profile. In contrast the flow in the back of the second wave does not converge to Nußelt state as clearly seen at $t = 140$ and 160 ms. Here the flow gains an excess of momentum near the free surface, as indicated by the large negative values of a_{dev} and also by the excess of velocity at the surface (compared to the Nußelt profiles) which increases from $t = 120$ to 140 ms. This observation can only be explained by lateral or longitudinal momentum transfer from adjacent fluid of higher velocity. The negative extreme of a_{dev} at the surface at $t = 160$ ms seems to be an effect of the approaching wave crest, which transfers momentum into the preceding film and causes a pressure gradient due to surface curvature and deflection of the streamlines. Both effects especially influence the region close to the film surface.

The overall flow conditions in Fig. 12 are characterised by an excess of momentum in the near wall region, as seen from the excess of velocity compared to the Nußelt profiles, from the rather large values of τ^*_w compared to τ_{w^*Nu} and from the predominance of negative deviation parameters a_{dev}. This may be a consequence of the selection of the present sequence due to its high density of large waves, which a priori involves a flow rate increased above the statistical mean. A second reason is the circumferential momentum transfer within three-dimensional

waves, which accelerates the flow at the side of the tip area of streak-like waves. It is highly probable, that the present measurements were performed at the lateral flanks of the waves, since the tip areas are rather small compared to the overall wave sizes as seen in Fig. 9.

At a higher flow rate, $Re_f = 77$ ($\dot{m}' = 0.126$ kg/s m), a similar sequence was recorded and is shown in Fig. 13. Three large waves, similar in thickness, $\delta_f = 0.6$–0.62 mm and velocity, $u_s = 0.74$–0.8 m/s, pass the measurement area at t = 40, 160 and 300 ms. They mainly differ in the shape of their back region. The waves at t = 40 and 300 ms decrease rapidly in thickness, whereas the wave at t = 160 ms exhibits a secondary crest at t = 220 ms. Probably two subsequent streak-like waves are observed during this time interval, comparable to those shown in Fig. 10, sequence I, near the frame centre at t = 160 ms.

The film flow at $Re_f = 77$ exhibits the same characteristics as that at $Re_f = 30$. Within the wave crests the flow velocity is about 50% smaller than in the corresponding Nußelt profiles. In the wave backs the measured profiles show higher velocities than the Nußelt profiles. This effect increases towards the end of the wave back, where $\delta_f < 0.3$ mm, as seen at t = 60 and 240 ms. At these instances the local mass flow rates $\dot{m}'^*$ exceed the corresponding Nußelt values $\dot{m}^*_{Nu}$ by up to 100%. The maximum wall shear stress τ^*_w is observed in the wave back of

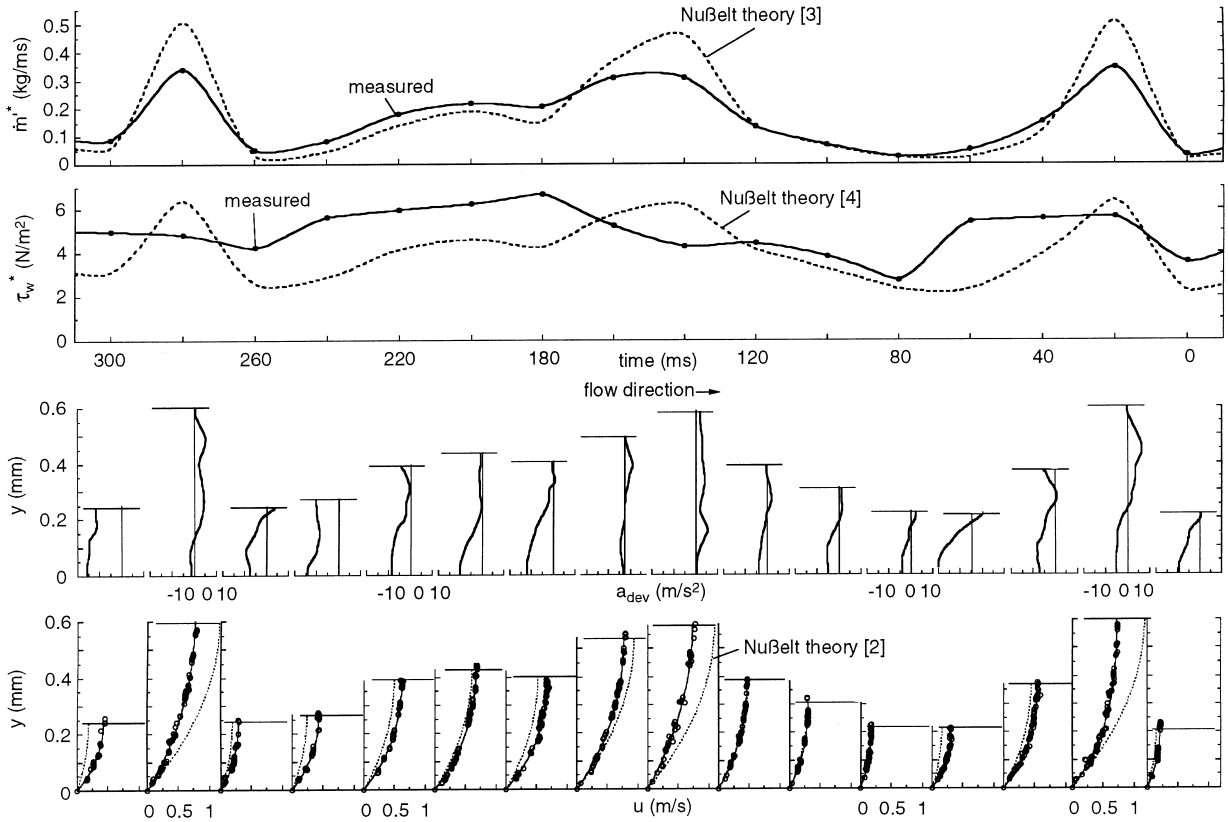

Fig. 13. Profiles of velocity u compared to the corresponding Nußelt profiles Eq. (2), profiles of deviation parameter a_{dev} and the comparison between the local mass flow rate $\bar{m}'^*$ and wall shear stress τ^*_w to the corresponding $\bar{m}^*_{Nu}$ and τ_{w^*Nu}, as calculated from Nußelt theory Eqs. (3) and (4) in their temporal development at $Re_f = 77$.

the large waves. As argued above, the temporal delay between the occurrence of the maximum surface velocity and the maximum wall shear stress can be explained by inertia effects of the flow adjacent to the wall.

It is worth noting, that the two-dimensional numerical results of Stuhlträger et al. (1995) reveal a similar flow pattern at $Re_f \approx 95$, where the flow in the wave crest is significantly slower compared to Nußelt profiles, whereas the velocities are larger in the wave back. Unfortunately, the data they present do not allow to obtain the location of the maximum τ_w^* with sufficient precision. An increase of τ_w^* in the wave back has been numerically predicted by Yu et al. (1995) for $Re_f = 150$. However, they obtained the maximum value of τ_w^* in the substrate film region. Experimentally the delayed occurrence of the maximum velocity gradient at the wall has been observed in the back of two-dimensional waves at significantly smaller $Re_f < 40$ by Alekseenko et al. (1994).

The PIV-sequence shown in Fig. 13 was selected due to their high density of large waves. Similarly to the situation at $Re_f = 30$, this could explain the predominance of negative a_{dev} in the wall region. To exclude such effects, a frame sequence mainly consisting of thin film has been evaluated and the results are shown in Fig. 14. The two large waves at the beginning

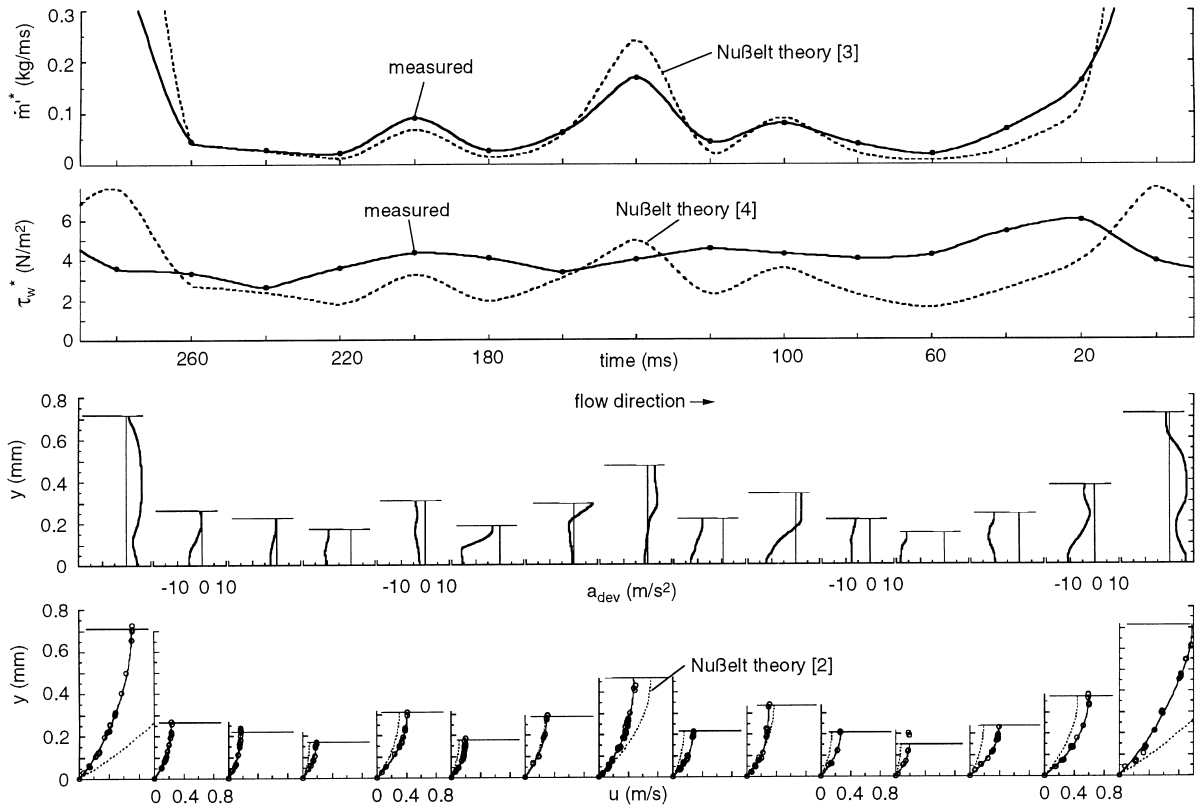

Fig. 14. Profiles of velocity u compared to the corresponding Nußelt profiles Eq. (2), profiles of deviation parameter a_{dev} and the comparison between the local mass flow rate $\bar{m}'^*$ and wall shear stress τ_w^* to the corresponding $\bar{m}_{Nu}^*$ and τ_{w^*Nu}, as calculated from Nußelt theory Eqs. (3) and (4) in their development in time at $Re_f = 77$.

and the end of this sequence are slightly larger than those observed in Fig. 13 ($\dot{m}'^{*}=0.49$ and 0.37 kg/s m with $\dot{m}^{*}_{Nu}=0.87$ and 0.85 kg/s m at $t = 0$ ms and $t = 280$ ms, respectively). In between them, a large area of thin film ranging from $\delta_f=0.15$ to 0.33 mm is observed, disrupted by one comparatively small wave, $\delta_f=0.47$ mm at $t = 140$ ms. At the crest of all three waves the measured velocities are significantly smaller than the corresponding Nußelt profiles, whereas they are higher in the wave back. These observations are identical to those mentioned above.

Major parts of the thin film are in a distorted state compared to the Nußelt theory, characterised by an excess of velocity and wall shear stress and by a predominance of negative values of the deviation parameter a_{dev}. These effects are not only observed in the back of the first large wave at $t = 20$–80 ms, but also at $t = 120$, 180 and 220 ms. There are only a few instances at $t = 200$, 240 and 260 ms, where the measurements coincide with the Nußelt profiles.

This experimental evidence questions the assumption of Nußelt velocity distribution in the residual film as made in several theoretical approaches. Furthermore, the observed flow distortion can be expected to increase heat and mass transfer in the residual film area due to

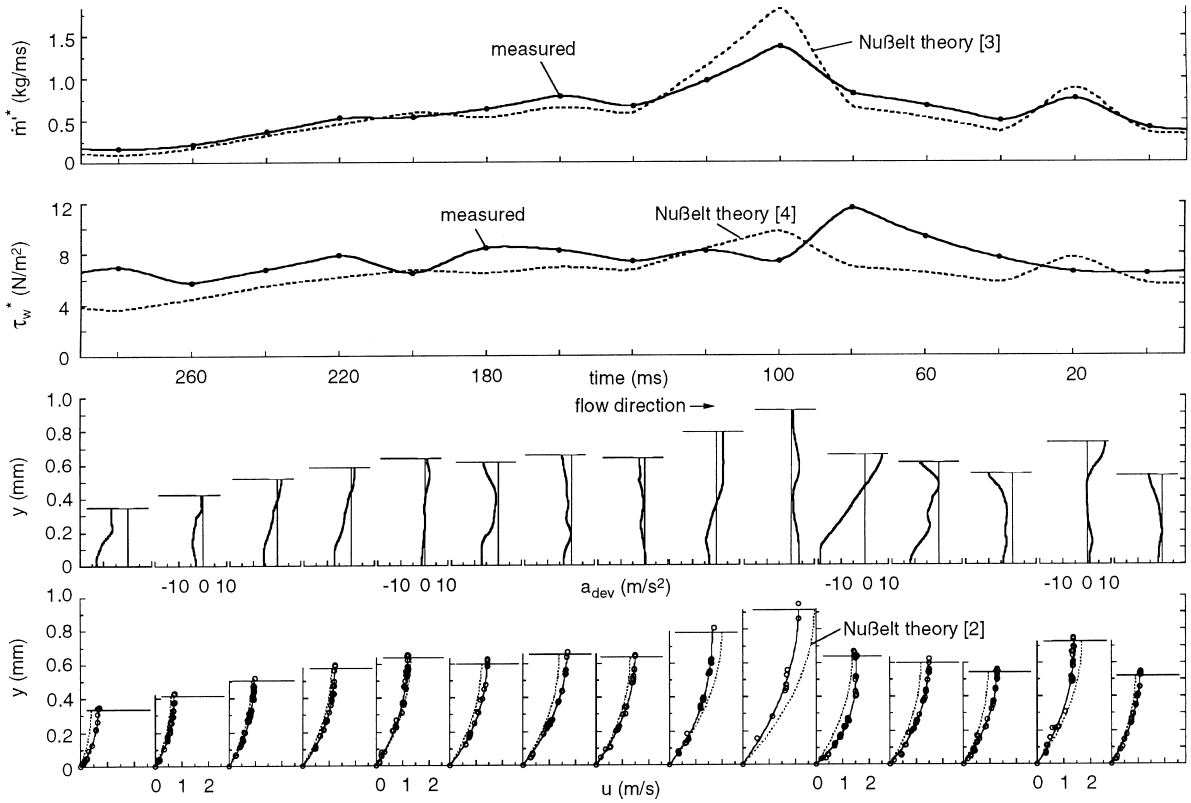

Fig. 15. Profiles of velocity u compared to the corresponding Nußelt profiles Eq. (2), profiles of deviation parameter a_{dev} and the comparison between the local mass flow rate $\bar{m}'^{*}$ and wall shear stress τ_w^{*} to the corresponding $\bar{m}^{*}_{Nu}$ and $\tau_{w^{*}Nu}$, as calculated from Nußelt theory Eqs. (3) and (4) in their development in time at $Re_f=200$.

enhanced convective transport. This may have a comparable effect on the overall transfer rates as the convective motion inside the large waves. Wasden and Dukler (1990) in their numerical investigation attempted to predict mass transfer rates considering the flow pattern in steady and interacting waves assuming that the residual film in between the waves to be in the equilibrium state according to Nußelt theory. Although this method narrows the gap between predictions and measurements it still underpredicts comparable measurements under certain conditions. This difference would decrease by taking the hydrodynamic distortion of the residual film into consideration.

At higher flow rates the wave patterns change drastically, as the film is increasingly dominated by streak-like waves, which line up in the wake of each other, as observed in sequence II of Fig. 11. Results of a PIV-sequence recorded at $Re_f = 200$ ($\dot{m}' = 0.328$ kg/s m) are given in Fig. 15, during which two waves are observed. The first, passing the measurement area at $t = 20$ ms, has a shape and thickness, $\delta_f = 0.74$ mm, which is still comparable to those at smaller Re_f, whereas the second wave reaches a thickness of $\delta_f = 0.87$ mm and a maximum velocity of $u_s = 2.27$ m/s, which corresponds to an instantaneous mass flow rate of $\dot{m}'^* = 1.37$ kg/sm. Furthermore, it exhibits an extremely long wave back with a secondary maximum of δ_f and $\dot{m}'^*$ at $t = 160$ ms. This secondary maximum belongs to a second smaller wave sliding down in the wake of the large wave at $t = 100$ ms. A comparable wave, marked C, is shown in Fig. 11, sequence II. The average mass flow rate $\dot{m}^*_{av} = 0.624$ kg/sm during the entire PIV-sequence is almost the double of the value obtained from the flow rate measurement. This is obviously caused by the inhomogeneous mass distribution due the line-up of streak-like waves.

Generally, the deviations between the experimental and the Nußelt profiles are small compared to those observed at smaller Reynolds numbers. The only exception is found at $t = 80$ ms, where the velocity profile appears non-parabolic exhibiting a steep gradient at the wall and a constant velocity region near to the free surface $y > 0.4$ mm. This type of profile is singular and may be caused by a turbulent region near the free surface.

5. Conclusions

The flow conditions of wavy laminar films have been investigated experimentally at the inner wall of a vertical tube at film Reynolds numbers ranging from $Re_f = 27$ to 200. A fluorescence intensity imaging technique is used to continuously measure the film thickness distribution in an area of 30×200 mm^2, enabling the observation of the transient behaviour of three-dimensional waves. In separate experiments the velocity distribution within the wavy film is measured by particle image velocimetry (PIV). These two methods allow to gain significant information on the flow field and on the surface structure of three-dimensional wavy falling films.

Throughout the flow range investigated, the wave structure is three-dimensional and affected by wave interactions. At low flow rates, $Re_f \approx 30$, interactions mainly occur between waves and substrate film, leading to wave deformation and circumferential wave mass transport, whereas direct wave–wave interactions are rare and hardly affect the average wave properties. Most waves are comparable in size and thickness, since merged waves tend to disintegrate shortly after their collision.

Direct wave–wave interactions gain importance at higher flow rates and lead to the formation of elongated streak-like waves. At $Re_f \approx 75$ wave collisions occur frequently, since the waves develop a higher velocity when sliding onto the accelerated wake of their predecessors, which results in subsequent collisions. Thereby mass accumulation causes large surge-like waves to originate. In the moment when such large and rapid waves are decelerated by direct interaction with slow substrate film, turbulent spots are induced. However, at $Re_f \approx 75$ such turbulent spots are singular events and relaminarise rapidly.

At higher flow rates, $Re_f \approx 200$, the film is characterised by consecutive streak-like waves with a high rate of wave interactions, which frequently induce the formation of turbulent spots. Due to wake effects the waves tend to line up, which locally causes a non-homogeneous film mass distribution in consecutive streak-like waves and rather large vertically stretched areas of residual film in between them.

Throughout the entire range of Reynolds numbers investigated here the velocity profiles obtained by PIV-measurements are of parabolic type. Some characteristics common to all waves are observed. The flow in the wave crest is in a decelerated state, whereas the wave back exhibits an excessive velocity compared to Nußelt theory. This effect in conjunction with the occurrence of the maximum wall shear stress in the wave back can be explained by the duration of momentum transport from the high velocity region at the wave top into the near wall region. As discussed above these observations agree well with previous experimental and numerical investigations and question the assumption that τ_w reaches a maximum directly underneath the wave crest as encountered in models based on self-similar velocity profiles and in the steady-state wave model of Brauner (1989). Furthermore, the thin substrate film between the waves hardly reaches an equilibrium state of viscous and gravity forces balancing each other, but exhibits an excess of momentum originating from interactions with the waves. Hence the assumption of Nußelt velocity distribution in the residual film area as used by several theoretical approaches seems questionable.

Strong velocity profile deformation as postulated by Brauner (1989) to occur in roll waves, where the surface flow velocity at the wave crest exceeds the wave propagation velocity, has not been observed experimentally. The measured profiles agree far better to their predictions of velocity distributions for non-rolling waves. In general this supports the assumption that roll waves are unlikely to develop in three-dimensional waves. However, to prove exactly that there is no occurrence of roll waves under the flow conditions investigated here, simultaneous measurements of surface and wave propagation velocity would be necessary.

As a general conclusion, it is to be stressed that both three-dimensionality and wave interactions strongly affect the flow structure throughout the entire range of Re_f investigated here. These effects are not adequately accounted for in current theoretical models of wave hydrodynamics, and should be included in future theoretical approaches. Regarding future experimental investigations, flow field measurement methods should be improved in time resolution and accompanied by simultaneous surface structure measurements in order to obtain a clear correlation between internal flow field and wave surface structure. Furthermore, it is feasible to quantify the role of wave interactions by statistical approaches, correlating wave shapes, distances and propagation velocities to obtain wave collision probabilities. These quantities could be useful to improve heat and mass transfer models based on statistical flow properties, e.g. the surface renewal and the penetration theory.

Acknowledgements

Financial support from the Deutsche Forschungsgemeinschaft (German Research Foundation) is gratefully acknowledged.

References

Adomeit, P., 1996. Experimentelle Untersuchung der Strömung laminar-welliger Rieselfilme. Ph.D. thesis, RWTH, Aachen.

Alekseenko, S.V., Nakoryakov, V.Y., Pokusaev, B.G., 1985. Wave formation on vertical falling liquid film. AIChE J. 31 (9), 1446–1460.

Alekseenko, S.V., Nakoryakov, V.Y., Pokusaev, B.G., 1994. Wave flow of liquid films. Begell House, New York.

Bach, P., Villadsen, J., 1984. Simulation of the vertical flow of a thin, wavy film using a finite-element method. Int. J. Heat Mass Transfer 27 (6), 815–827.

Banerjee, S., Rhodes, E., Scott, D.S., 1967. Mass transfer to falling wavy liquid films at low Reynolds numbers. Chem. Eng. Sci. 22, 43–48.

Brauner, N., Maron, M.D., 1983. Modelling of wavy flow in inclined thin films. Chem. Eng. Sci. 38, 293–302.

Brauner, N., Maron, M.D., 1987. Characterisation of the interfacial velocity in wavy thin film flow. Int. Comm. Heat Mass Transfer 14, 293–302.

Brauner, N., 1989. Modelling of wavy flow in turbulent free falling films. Int. J. Multiphase Flow 15 (4), 505–520.

Chen, L.-H., Chang, A.J., 1986. Nonlinear waves on liquid film surfaces. II. Bifurcation of the long wave equation. Chem. Eng. Sci. 41, 2477–2486.

Hagiwara, Y., 1989. Numerical analysis of 3D interfacial shape and velocity distribution of liquid film. PCH 11 (1), 49–62.

Henstock, W.H., Hanratty, T.J., 1978. Gas absorption by a liquid layer flowing on the wall of a pipe. AIChE J. 25 (1), 122–131.

Ho, F.C.K., Hummel, R.L., 1970. Average velocity distribution within falling liquid films. Chem. Eng. Sci. 25, 1225–1237.

Ho, L-W., Patera, A.T., 1990. A Legendre spectral element method for simulation of unsteady incompressible viscous free-surface flows. Comp. Methods Appl. Mech. Eng. 80, 355–366.

Liu, J., Paul, J.D., Gollup, J.P., 1993. Measurements of primary instabilities of film flows. J. Fluid Mech. 250, 69–101.

Karapantsios, T.D., Paras, S.V., Karabelas, A.J., 1989. Statistical characteristics of free falling films at high Reynolds numbers. Int. J. Multiphase Flow 15, 1–21.

Karapantsios, T.D., Karabelas, A.J., 1995. Longitudinal characteristics of wavy falling films. Int. J. Multiphase Flow 21, 119–127.

Kheshgi, H.S., Scriven, L.E., 1987. Disturbed film flow on a vertical plate. Phys. Fluids 30 (4), 990–997.

Mudawar, I., Houpt, R.A., 1993. Measurements of mass and momentum transport in wavy-laminar falling liquid films. Int. J. Heat Mass Transfer 36, 4151–4162.

Nakoryakov, V.Y., Pokusaev, B.G., Alekseenko, S.V., Orlov, V.V., 1977. Instantaneous velocity profile in a wavy fluid film. J. Eng. Sci. 33, 1012–1016.

Nußelt, W., 1916. Die Oberflächenkondensation des Wasserdampfes I, II. Z.VDI 60, 541–546 and 569–575.

Portalski, S., Clegg, A.J., 1972. An experimental stuy of wave inception on falling liquid films. Chem. Eng. Sci. 27, 1257–1265.

Seban, R.A., Faghri, A., 1978. Wave effects on the transport to falling laminar liquid films. J. Heat Transfer 100, 143–147.

Semena, M.G., Mel'nichuk, G.A., 1978. Mean-velocity distributions in a falling film. Fluid Mech. Sov. Res. 7, 145–151.

Stuhlträger, E., Naridomi, Y., Miyara, A., Uehara, H., 1993. Flow dynamics and heat transfer of a condensate film on a vertical wall. I. Numerical analysis and flow dynamics. Int. J. Heat Mass Transfer 36 (6), 1677–1686.

Stuhlträger, E., Miyara, A., Uehara, H., 1995. Flow dynamics and heat transfer of a condensate film on a vertical wall. II. Flow dynamics and heat transfer. Int. J. Heat Mass Transfer 38 (15), 2715–2722.

Takahama, H., Kato, S., 1980. Longitudinal flow characteristics of vertically falling liquid films without concurrent gas flow. Int. J. Multiphase Flow 6, 203–215.

Trifonov, Y.Y., Tsvelodub, O.Y., 1991. Nonlinear waves on the surface of a falling liquid film. Part 1. Waves of the first family and their stability. J. Fluid Mech. 229, 531–554.

Wasden, K.F., Dukler, A.E., 1990. A numerical study of mass transfer in free falling wavy films. AIChE J. 36 (9), 1379–1390.

Wehausen, J.V., Laitone, E.V. 1960. Surface waves. In: Flügge, S., Truesdell, C. (Eds.), Handbuch der Physik. Springer Verlag, Berlin.

Wilkes, J.O., Nedderman, R.M., 1962. The measurement of velocities in thin liquid films. Chem. Eng. Sci. 17, 177–186.

Yu, L.Q., Wasden, K.F., Dukler, A.E., Balakotaiah, V., 1995. Nonlinear evolution of waves on falling films at high Reynolds numbers. Phys. Fluids 7, 1886–1902.